Clim. Past Discuss., 11, 3375–3424, 2015
www.clim-past-discuss.net/11/3375/2015/
doi:10.5194/cpd-11-3375-2015

Climate of the Past Discussions

The influence of tropical volcanic eruptions on the climate of South America during the last millennium

C. M. Colose[1], **A. N. LeGrande**[2], **and M. Vuille**[1]

[1]Dept. of Atmospheric and Environmental Sciences, University at Albany, SUNY, Albany, NY 12222, USA
[2]NASA Goddard Institute for Space Studies, New York, NY, 10025, USA

Received: 08 June 2015 – Accepted: 14 June 2015 – Published: 23 July 2015

Correspondence to: C. M. Colose (ccolose@albany.edu)

Published by Copernicus Publications on behalf of the European Geosciences Union.

Abstract

Currently, little is known on how volcanic eruptions impact large-scale climate phenomena such as paleo-ITCZ position or South American summer monsoon behavior. In this paper, an analysis of observations and model simulations is employed to assess the influence of large volcanic eruptions on the climate of South America. This problem is considered both for historically recent volcanic episodes, for which more comprehensive global observations exist, as well as reconstructed volcanic events for the period 850 C.E. to present that are incorporated into the NASA GISS ModelE2-R simulation of the Last Millennium. An advantage of this model is its ability to explicitly track water isotopologues throughout the hydrologic cycle and simulating the isotopic imprint following a large eruption. This effectively removes a degree of uncertainty associated with error-prone conversion of isotopic signals into climate variables, and allows for a direct comparison between GISS simulations and paleoclimate proxy archives.

Our analysis reveals that both precipitation and oxygen isotope variability respond with a distinct seasonal and spatial structure across South America following an eruption. During austral winter, the heavy oxygen isotope in precipitation is enriched, likely due to reduced moisture convergence in the ITCZ domain and reduced rainfall over northern South America. During austral summer, however, precipitation is depleted in heavy isotopes over Amazonia, despite reductions in rainfall, suggesting that the isotopic response is not a simple function of the "amount effect". During the South American monsoon season, the amplitude of the temperature response to volcanic forcing is larger than the rather weak and spatially less coherent precipitation signal, potentially masking the isotopic response to changes in the hydrologic cycle.

1 Introduction

1.1 Volcanic forcing on climate

Plinian (large, explosive) volcanic eruptions are a dominant driver of naturally forced climate variability during the Last Millennium (LM, taken here to be 850 C.E. to present; e.g., Stothers and Rampino, 1983; Hansen et al., 1992; Crowley et al., 2000; Robock et al., 2000; Robock, 2003; Goosse et al., 2005; Yoshimori et al., 2005; Emile-Geay et al., 2008; Cole-Dai, 2010; Timmreck, 2012; Iles et al., 2013; Schurer et al., 2014). In addition to their importance for 20th century climate, they are likely the most important external forcing during last 1000 years of the pre-industrial period, the most recent key interval identified by the Paleoclimate Modelling Intercomparison Project Phase III (PMIP3). As such, these eruptions serve as a natural testbed to assess the skill of climate models in simulating how climate responds to external perturbations.

Although the most significant climate impacts of eruptions are expressed over just a few years following the eruption, they provide the source of the largest amplitude perturbations to Earth's energy budget during the LM. For example, the eruption of Mt. Pinatubo in June 1991, although transitory, exerted a radiative forcing comparable to an instantaneous halving of atmospheric CO_2 (Hansen et al., 1992; Minnis et al., 1993; see also Driscoll et al. (2012) for models in the Coupled Model Intercomparison Project Phase 5, CMIP5); several paleo-eruptions during the LM likely had an even larger global impact (Fig. 1).

The principle climate impact from volcanic eruptions results from the liberation of sub-surface sulfur-containing gases such as sulfur dioxide and hydrogen sulfide, which are injected into the stratosphere and can react with water to form sulfate (75 % H_2SO_4) aerosols (e.g., Harshvardhan and Cess, 1976; Coakley and Grams, 1976; Pollack et al., 1976, 1981; Lacis et al., 1992). The most pronounced impact of large tropical eruptions includes a radiatively cooled troposphere and heated stratosphere (e.g., Lacis et al., 1992; Robock and Mao, 1995; Stenchikov et al., 1998). Sulfate aerosols from the Mt. Pinatubo eruption had an effective radius of up to $\sim$ 0.5–0.8 µm, comparable in size

to a visible wavelength and strongly scattering to incoming solar radiation. Unless the particles can reach sizes larger than $\sim$ 1–2 µm, this scattering more than offsets the small increase in infrared opacity from the aerosols, and results in a cooling of Earth's surface (Turco et al., 1982; Lacis et al., 1992). The stratospheric warming is caused by absorption of near-infrared and longwave radiation, and results in anomalous temperature gradients between the equator and poles, and an enhancement of the polar vortex. This typically results in warming over sectors of the northern mid-latitudes during boreal winter (e.g., Robock and Mao, 1992; Kirchner et al., 1999; Shindell et al., 2004; Stenchikov et al., 2004, 2006).

Studies on the impacts of volcanic eruptions have generally focused on global or Northern Hemisphere metrics (e.g., Lucht et al., 2002; Gillett et al., 2004; Shindell et al., 2004; Oman et al., 2005, 2006; Anchukaitis et al., 2010; Peng et al., 2010; Evan et al., 2012; Zhang et al., 2013; Man et al., 2014), for instance in examining responses to the East Asian monsoon system (EAMS) or the Arctic Oscillation. Comparatively little attention has been given to the Southern Hemisphere, or to South America specifically (although see Joseph and Zeng, 2011, and Wilmes et al., 2012). Some previous work has focused on the Southern Annular Mode in the ERA-40 and NCEP/NCAR reanalysis, in addition to a previous version of NASA Goddard Institute for Space Studies (GISS) Model-E (Robock et al., 2007) and in a subset of CMIP3 models (Karpechko et al., 2010) or in CMIP5 (Gillett and Fyfe, 2013).

How volcanic forcing is expressed over South America remains an important target question for several reasons. First, recognition of the South American monsoon system (SAMS) as an actual monsoon system is less than two decades old (Zhou and Lau, 1998), and thus study of SAMS dynamics is still relatively young (Sect. 1.3) and very little work has been done specifically focused on volcanic eruptions. For instance, should we expect to see a reduction in austral summer rainfall (during the monsoon season) as has been reported for the EAMS (Man et al., 2014)? Secondly, the largest volcanic eruptions during the late 20th century (e.g., Mt. Agung, 1963, Indonesia; El Chichón, 1982, Mexico; Mt. Pinatubo, 1991, Island of Luzon in the Philippines – hereafter, L20

eruptions) occur quasi-simultaneously with an anomalous El Niño–Southern Oscillation (ENSO) state, thus limiting the prospect of robust hypothesis-testing and guidance for what impacts ought to be expected following large eruptions. Finally, South America offers promise for a comparatively dense network of high-resolution proxy locations relative to other tropical regions (see below), offering the potential to detect whether South American hydroclimate signals to large eruptions are borne out paleoclimatically.

In this study, we will explore the post-volcanic response of South American climate operating through the vehicle of unique model simulations (spanning the LM) using the recently developed GISS ModelE2-R (LeGrande et al., 2015; Schmidt et al., 2014a), which allows for the sampling of a greater number of events than is possible over the instrumental period. Emphasis is placed on temperature and precipitation, but a novel part of this study extends to the response of water isotopologues (e.g., $H_2^{18}O$) (colloquially referred to hereafter as "isotopes" and expressed as $\delta^{18}O$ in units per mil (‰) vs. Vienna Standard Mean Ocean Water). The isotopic composition of precipitation ($\delta^{18}O_p$) is a key variable that is directly derived from proxy data used in tropical paleoclimate reconstructions.

The aim of this paper is to create a potentially falsifiable prediction for the isotopic imprint that a volcanic eruption should tend to produce across the South American continent. The ability to explicitly model the isotopic response allows for a less ambiguous comparison of simulations and paleoclimate archives and for hypothesis testing. It is unclear whether or not the current proxy archives are suitable to test such a prediction given dating uncertainties, resolution, or the high level of noise in proxy data. Additionally, the prevailing high-resolution archives in South America only feature a few tropical records (Vimeux et al., 2009; Neukom and Gergis, 2012; Vuille et al., 2012). Nonetheless, the growing number of high-resolution archives offers hope that testing the modeled response to high-frequency volcanic signals will be an avenue for future research. This can also better inform debate centered on the inverse problem in interpreting isotopic signals (i.e., what do observed changes in proxy data imply about past climate changes?), which remains contentious (Sect. 1.4).

The structure of this article is as follows: in the remaining part of Sect. 1, we summarize previous literature on the impact of large volcanic eruptions on paleoclimate, in addition to a discussion of South American climate. Section 2 presents data and methodology, including how volcanic forcing is implemented in ModelE2-R. Section 3 discusses our results and we end with some conclusions in Sect. 4.

1.2 Volcanic forcing during the last millennium

Volcanic forcing has had a very large influence on the climate of the LM (Crowley, 2000; Hegerl et al., 2003, 2006; Shindell et al., 2004; Mann et al., 2005; Fischer et al., 2007; D'Arrigo et al., 2009; Timmreck, 2012; Esper et al., 2013; Ludlow et al., 2013; Schurer et al., 2014). Several studies (Miller et al., 2012; Schurer et al., 2014) collectively provide a compelling case that volcanic forcing may be substantially more important than solar forcing on a hemispheric-to-global scale during the LM, in addition to driving a large portion of the inter-annual to multi-decadal variability in LM simulations (Schmidt et al., 2014b).

For the LM, it is necessary to use measurements of the total acidity or the sulfate content in ice cores for a reconstruction of the incidence of explosive volcanism (e.g., Hammer, 1980; Crowley et al., 1993; Robock and Free, 1995; Zielinski et al., 1995; Zielinski, 2000). Two volcanic forcing datasets (Gao et al., 2008; Crowley and Unterman, 2013) relying on ice core reconstructions of volcanism are used as input in the LM ModelE2-R simulations, as discussed in Sect. 2.

1.3 South American climate

South America is home to nearly 390 million people. The continent spans a vast meridional extent (from $\sim 10^{\circ}$ N to 55° S), contains the world's largest rainforest (the Amazon), in addition to a rather Mars-like desert (Atacama) that competes only with the dry valleys of Antarctica for the driest location on Earth. The continent has diverse orography, spanning the high Andes along the Pacific to Laguna del Carbón in Argentina, the

lowest point in the Southern Hemisphere. Because of this, South America hosts a rich diversity of climate zones and biodiversity, all of which may respond in unique ways to external forcing.

The most prominent climatic feature of tropical and subtropical South America is the South American monsoon system (Zhou and Lau, 1998; Marengo et al., 2001, 2012; Vera et al., 2006; Garreaud et al., 2009). Much of South America is in a monsoon regime, with tropical/subtropical rainfall over the continent exhibiting a pronounced seasonal cycle. Unlike other monsoon systems such as that in Asia, low-level easterly winds prevail during the entire year in tropical South America, although the wind anomalies do change direction when the annual mean wind field is removed from winter and summer composites (Zhou and Lau, 1998).

During austral winter, the maximum in continental precipitation is largely restricted to north of the equator, in a band-like pattern associated with the oceanic Inter-tropical Convergence Zone (ITCZ). During austral summer, convection is displaced from northwestern South America, and a band of heavy precipitation covers much of the continent, from the southern Amazon Basin to central Brazil and northern Argentina. A distinctive feature of the SAMS is the South Atlantic Convergence Zone (SACZ), a band of cloudiness and precipitation sourced primarily from the tropical Atlantic that extends diagonally (southeastward) from the Amazon towards southeastern Brazil (Fig. 2).

The SAMS onset occurs around the end of October and the demise between the end of March and April (e.g., Nogués-Paegle et al., 2002; Vera et al., 2006; Silva and Carvalho, 2007). The dominant mode of intraseasonal precipitation variability over South America during summer exhibits a dipole pattern (Nogués-Paegle and Mo, 1997), seesawing between the SACZ region and Southeastern South America (SESA), the latter including the densely populated La Plata basin with local economies strongly dependent on agricultural activities.

The SAMS is strongly modulated by ENSO behavior on inter-annual timescales (Vuille and Werner, 2005; Garreaud et al., 2009). In general, tropical South America tends to experience drier than normal conditions during El Niño, while conditions in

subtropical latitudes are anomalously humid, including the southeastern part of the continent. Surface air temperatures tend to be anomalously warm in tropical and subtropical South America during El Niño events. These relationships depend somewhat on the time of year, and during La Niña events, the pattern is essentially reversed.

1.4 Recent South American monsoon reconstructions from isotopic proxies

SAMS variability spanning most of the Holocene has been diagnosed from speleothem records in the Peruvian Andes (Kanner et al., 2013) and a review focused on the last 1000–2000 years was given in Bird et al. (2011) and Vuille et al. (2012). In all cases, a critical piece of information that is required to properly diagnose paleo-SAMS variability is the ability to translate oxygen isotope variability from natural archives into a physical climate signal of interest.

Early work on isotopes in ice core records from the tropical Andes detected a Little Ice Age (LIA) signal in the oxygen isotope composition of the ice, with results initially interpreted to reflect variations in local temperature due to their resemblance to ice core records from Greenland (e.g., Thompson et al., 1995, 1998) and due to their isotopic enrichment over the past 150 years, in parallel with rising global mean temperatures (Thompson et al., 2006). A temperature-dependence to oxygen isotope variability has been long known and is particularly important in mid-to-high latitudes (Dansgaard, 1964) and is most directly related to the ratio of initial and final water vapor content of a parcel that is transported horizontally, rather than the temperature-dependence of fractionation itself (Hoffman and Heimann, 1997).

This interpretation in the tropics has been challenged through a number of observational and modeling efforts (Hardy et al., 2003; Vuille and Werner, 2005; Vimeux et al., 2005, 2009; Kanner et al., 2012) which suggest that isotopic signal is more closely related to the degree of rainout upstream in regions of intense convection (in the case of South America, over the Amazon Basin). Additionally, since sea surface temperatures (SST) in the Pacific have a large influence on SAMS intensity on inter-annual timescales in the present, oxygen isotope variability over much of tropical South Amer-

ica is linked to the state of the equatorial Pacific (Bradley et al., 2003; Vuille et al., 2003).

In regimes that are highly convective in nature as in tropical South America, empirical evidence shows that the amount of precipitation (the so-called "amount effect") rather than the condensation temperature correlates most strongly with $\delta^{18}O_p$ variability, at least on seasonal to inter-annual time scales. In reality, however, the rainout most relevant for the oxygen isotope signal may be a significant distance from the site where the proxy is derived, potentially complicating the use of local calibrations to climatology as a guide for $\delta^{18}O_p$ interpretations (Schmidt et al., 2007). Isotopic concentrations are explainable as being a function of original concentration, rainout along the moisture transport path, and mixing.

The influence of precipitation amount on $\delta^{18}O_p$, in addition to changes in the partitioning of precipitation sources, has also been identified on decadal to orbital timescales through speleothem records and lake sediments (Cruz et al., 2005; Van Breukelen et al., 2008; Bird et al., 2011; Kanner et al., 2012). These studies have also highlighted the role of latitudinal displacements of the ITCZ, which is ultimately the main moisture conduit for precipitation over the South American continent. Furthermore, many records collected throughout South America now provide evidence for enriched $\delta^{18}O_p$ values during the Medieval Climate Anomaly, which is indicative of weakened SAMS convection and rainout, followed by depleted $\delta^{18}O_p$ values, suggesting heavier rainfall during the LIA in tropical South America (Bird et al., 2011; Apaestegui et al., 2014) with an opposite response in Northeast Brazil (Novello et al., 2012). This, in turn, has been interpreted in terms of North Atlantic SST anomalies (Vuille et al., 2012; Ledru et al., 2013) and the position of the Atlantic ITCZ.

Nonetheless, oxygen isotopes respond in unique ways depending on the climate forcing of interest. Indeed, a unique, quantitative local relationship between an isotope record and any particular climate variable of interest is unlikely to hold for all timescales and prospective forcing agents (Schmidt et al., 2007) thus motivating the use of forward

modeling to work in conjunction with proxy-based field data. For the remainder of this paper, we focus specifically on the volcanic forcing response.

2 Methodology

2.1 Data

The primary tool used in this study is the water isotope-enabled GISS ModelE2-R. ModelE2-R is a fully coupled atmosphere–ocean GCM (LeGrande et al., 2015; Schmidt et al., 2014a) that explicitly tracks stable water isotopes. The version used here is the same as the non-interactive atmospheric composition (NINT) physics version used in the CMIP5 experiments. The current model features 2° latitude × 2.5° longitude horizontal resolution and 40 vertical levels in the atmosphere up to 0.1 hPa, and is coupled to the Russell Ocean that conserves heat, water mass, and salt (Russell et al., 1995) at 1° × 1.25° resolution with 32 vertical levels. ModelE2-R includes stratospheric dynamics and prescribed ozone and aerosol species.

Due to uncertainties in past radiative forcing, a suite of LM simulations using ModelE2-R have been run with different combinations of plausible solar, volcanic, and anthropogenic land use histories (Schmidt et al., 2011, 2012) but with identical greenhouse gas and orbital evolution. These simulations span the period 850–2005 C.E. There are two reconstructions of past volcanic activity (Gao et al., 2008; Crowley and Unterman, 2013) that are used in the ModelE2 simulations. We focus only on results from the Crowley reconstruction prior to 1850 CE due to a mis-scaling of the Gao forcing in the model that roughly doubled the appropriate radiative forcing. For the historical period (1850-present), the volcanic forcing history is based on Sato et al. (1993) and is equivalent among the different simulation members.

For the LM, three forcing combinations are available in the GISS ModelE2-R simulations that use the Crowley reconstruction for volcanic perturbations. These include Pongratz et al. (2008) (land)/Krivova et al. (2007) (solar), Kaplan et al. (2010) (land)/Krivova

et al. (2007) (solar), and Pongratz et al. (2008) (land)/Steinhilber et al. (2009) (solar) (see Schmidt et al., 2011, 2012).

Water isotope tracers are incorporated into the model's atmosphere, land surface, sea ice, and ocean. These isotopes are advected and tracked through every stage of the hydrologic cycle. At each phase change (including precipitation, evaporation, ice formation or melting) an appropriate fractionation factor is applied (Schmidt et al., 2005) and all freshwater fluxes are tagged isotopically.

Crowley and Unterman (2013) discuss the details behind the LM Aerosol Optical Depth (AOD) reconstruction that defines the volcanic forcing time-series in ModelE2-R (Fig. 1). This estimate is derived from sulfate peaks in ice cores, which are relatively well dated and referenced to the historical record during the satellite era. Crowley and Unterman (2013) provide an AOD history over 4 latitude bands (from 0–30° and 30–90° in both hemispheres). ModelE2-R uses a cubic spline to interpolate this forcing dataset over 24 latitude bands. The choice of volcanic eruptions used for the LM analysis (Sect. 2.2 below) is based on the AOD dataset from this 24-latitude grid.

In addition to the model, we take advantage of the NASA GISS Surface Temperature analysis (GISTEMP) land-ocean index (Hansen et al., 1999), and a merged precipitation dataset using land gauges from 1948–1978 (Chen et al., 2002) and Global Precipitation Climatology Project (GPCP) v2.1 from 1979–present that also incorporates satellite data (Huffman et al., 2009). These datasets are called upon to gauge the spatial pattern and tropical mean climate response following the most recent two L20 eruptions (only land for Mt. Agung, since sufficient oceanic precipitation coverage is not obtainable before 1979).

The GPCP product offers considerably better global and South American coverage than other precipitation datasets, although observational density for rainfall is still considerably more problematic over South America than for many other regions of the globe. There is a sharp drop-off in the number of rain gauge stations used in the product prior to the 1950's over much of the South American continent. Figure S1 shows

the station density at the beginning month of each L20 eruption, and the total number of land stations over South America with time.

Finally, in Sect. 3.1 we present data from the Global Network of Isotopes in Precipitation (GNIP) accessible from the International Atomic Energy Agency (IAEA) for $\delta^{18}O_p$ as a test of the model's ability to track the seasonal hydrologic cycle in the form of its isotopic response over South America before discussing the Last Millennium results. Unfortunately, there is considerable spatial and temporal heterogeneity in the GNIP data over South America, and no isotopic measuring station over the continent exhibits the temporal continuity to assess the isotopic response to all three eruptions. In fact, only a few stations have data overlap with one or two eruptions and with a sufficient number of $\delta^{18}O_p$ data points to establish reasonable seasonal or annual statistics, ensuring little hope that the prevailing network of observations is suitable for hypothesis testing in our context. Because of this and the data drop-off in precipitation coverage, we do not examine observed South American hydroclimate responses to early 20th century eruptions.

2.2 Super-posed epoch and composite analysis

For the most recent two L20 eruptions, we present a composited tropical-mean (temperature and precipitation anomalies zonally averaged from 25° S to 25° N) super-posed epoch analysis. The GISTEMP product already provides data in the form of monthly anomalies, and the seasonal cycle was removed from the precipitation data at each grid cell. Results for the super-posed epoch analysis are baselined such that the data has zero mean during eight years from −3 to 5, with zero defining the eruption month of El Chichón and Mt. Pinatubo. Mt. Agung is excluded in this analysis as it occurs before the satellite era.

Additionally, we present the spatial pattern of observed and simulated response for temperature and precipitation for all three L20 eruptions. Results are shown for DJF and JJA with two 3 month segments for each season included in the post-volcanic response (e.g., Mt. Pinatubo erupted in June 1991, and so the JJA post-volcanic field

is shown for June–July–August 1991 and June–July–August 1992). The pre-eruption field subtracted from this includes the five years prior to the eruption. Other sensible choices for the non-eruption years (such as also using five years after the eruption or detrending the dataset and using a 30 year climatology, not shown) do not significantly change the results.

For the full LM spatial composites, eruptions are defined as points in which vertically integrated (15 to 35 km) stratospheric AOD averaged from 20° N to 30° S exceeds 0.1 for at least 12 consecutive months in the simulation (top panel in Fig. 1); this criterion yields 16 eruptions since 850 C.E. The selection of events used in the LM composite is very weakly sensitive to this choice of latitude band. A notable exception is El Chichón that was used in the L20 composites, but not for the LM, since this event is a "unipolar" eruption (Crowley and Unterman, 2013) in the sense that the largest AOD perturbation is confined to the Northern Hemisphere despite the eruption being of tropical origin. Mt. Agung and Mt. Pinatubo are actually the first and second smallest eruptions in this selection based on the maximum AOD encountered near the time of the eruption (see Table 1 for dates of each event).

For the LM "non-eruption" fields used as a reference period to calculate the anomaly for each event, months for 15 years on either side of each eruption are used, not including months in which the AOD exceeds 0.1, either for that eruption or any overlapping months from other eruptions (overlap occurs only once for eruptions in 1809 and 1815). When constructing seasonal averages of $\delta^{18}O_p$ in the model, the oxygen isotope value for each month is weighted by the precipitation amount during that month, at each grid cell.

Since each post-eruption difference field is computed using the immediate response minus a surrounding 30 year climatology, time is not relevant in this analysis and so we use all three ensemble members with the Crowley forcing to generate a composite that features 48 volcanic "events" (16 eruptions in each of the 3 members). For the model composites covering the L20 eruptions, the mis-scaling of the Gao forcing is not an issue, and so we use six ensemble members each. The ensemble-mean composite

results displayed for the LM/L20 eruptions include contributions from three/six members which differ not just in the internal variability, but also in their solar and land-use forcing. However, the primary signal of interest only lasts for a few years following an eruption and is expected to be large compared to the impact of more slowly varying and smaller-amplitude forcings. Therefore, the ensemble spread to a given eruption can be interpreted as a sampling of the model internal variability coincident with the event.

Finally, it is now well appreciated that any climate response under investigation will be slaved to the spatial structure of the forcing imposed on a model. For example, preferential heating/cooling of one hemisphere will induce different tropical precipitation responses than a well-mixed gas that behaves CO_2-like (Kang et al., 2008, 2009; Frierson and Hwang, 2012; Haywood et al., 2012). Figures S2 and S3 show the latitudinal AOD distribution structure for all eruptions used in the generation of the LM composites within ModelE2-R. The mean of all events is rather symmetric between hemispheres (though somewhat skewed toward the Southern Hemisphere tropics, which is linked to the selection criteria), and similar to the pattern expected with CO_2 change, the forcing is largest in the tropics. Thus, the resulting climate responses outlined in this paper ought to be viewed as a response consistent with a forcing that is relatively symmetric about the equator. Results from volcanic eruptions with emphasis on the spatial structure of forcing will be reported in a separate paper.

2.3 Influence of ENSO on the late 20th century (L20) eruptions

For all three volcanic events during the last 60 years, El Niño events are occurring quasi-simultaneously with the eruption. This introduces a pervasive issue when attempting to isolate the volcanic signal (e.g., Robock, 2003; Trenberth and Dai, 2007; Joseph and Zeng, 2011) and is particularly important over South America (e.g. Garreaud et al., 2009).

In order to remove the effects of ENSO from the super-posed epoch and spatial composite analyses described above in the GISTEMP and GPCP data, we first perform

a multiple regression with the variable of interest over the period 1951–2005 using a linear time trend and the Niño 3 index as predictors (5° N–5° S, 150–90° W, data from http://www.cpc.ncep.noaa.gov/data/indices/) over the same period, excluding two years of data after each L20 eruption. At each grid cell, the Niño 3 index is lagged from 0–6 months and the correlation coefficient with the maximum absolute value (since a positive index can induce a negative anomaly in the variable of interest) is found. This is similar to the approach used in Joseph and Zeng (2011), allowing the maximum ENSO influence to be removed at each grid point at different times. The lagged Niño index is then regressed against the time series of each variable and the residual from this regression is retained. This approach assumes a linear relationship between ENSO and the climate response over South America, an assumption that appears justified on inter-annual to decadal time scales (Garreaud et al., 2009).

For each of the six ensemble members used in the model L20 composite, a similar procedure is performed in which the Niño 3 index (consistent with the realization of the Niño 3 domain SSTs in that model simulation) is calculated and regressed out in the same manner. For the full LM computations, the large number of events in the three-ensemble member composite should help average out the influence of Pacific SST variability, and no ENSO removal procedure is applied.

3 Results and discussion

3.1 L20

Figure 3a and b shows the ENSO-removed super-posed epoch analysis for tropical temperature and precipitation associated with the recent two L20 eruptions. Both time-series series exhibit negative anomalies in the composite, although the precipitation response is noisier. There is good agreement between the observed and modeled temperature response, both in amplitude and recovery timescale. The precipitation signal displays a modest reduction in the composite, with the recovery in observations occur-

ring faster (between year 1 and 2) than in the model, although this behavior emerges from a different recovery pattern between El Chichón and Mt. Pinatubo (not shown). The peak monthly precipitation reduction is larger in both the observations and model for Mt. Pinatubo, consistent with a larger AOD perturbation.

The spatial structure of the late 20th century temperature and precipitation response for both solstice seasons in observations and the model (ensemble mean) are shown in Figs. 4 and 5, respectively. Observations exhibit cooling over much of the globe, especially after Mt. Pinatubo that is largely reproduced by the model. The model results are averaged over six ensemble members reducing the amplitude of some of the structure seen in observations, although many of the patterns observed are also borne out in the simulations. For instance, the JJA temperature expression over the United States is reproduced as a cooling after El Chichón and Mt. Pinatubo, with a warm anomaly in the middle and eastern part of the continent following Mt. Agung in both the model and observations. A wave-like dynamic warm pattern (discussed in Sect. 1.1) is observed during DJF in northern mid-latitudes, a pattern recovered in ModelE2-R. Widespread tropical African cooling is observed after Mt. Pinatubo in both seasons, and after El Chichón during boreal winter.

In GISTEMP, the high-latitudes of South America cool more than the tropical region of the continent for all observed cases except El Chichón during the DJF season, a pattern not reproduced by the model simulations. The largest differences often relate to the state of the Pacific. For example, there is a residual signal from ENSO following El Chichón that is not reproduced by the model. This would not be expected in a free-running coupled simulation. The magnitude of this signal is sensitive to the Niño index used in the regression method described above. Performing a regression procedure using other ENSO indices such as SST anomalies from the Niño 3.4 domain, Cold Tongue Index, or Multivariate Enso Index do not perform better in removing the East Pacific SST residual after El Chichón, although the linear regression approach performs well at removing ENSO signatures over the South American continent. With no ENSO removal procedure applied this East Pacific warm anomaly is much stronger

following El Chichón and becomes very apparent after Mt. Pinatubo as well, with relatively warm SSTs spanning nearly the entire tropical Pacific. Additionally, without ENSO removal, tropical South America warms following the two eruptions (not shown). The influence of ENSO appears minimal over the higher latitude sectors of the continent. Thus the comparison to the model in the South American tropics is connected to the ENSO state and the removal procedure employed.

The precipitation pattern after all three L20 eruptions exhibits substantial variability in space and across eruptions, with a general drying pattern over land in tropical latitudes and further evidence of imperfect ENSO removal in the Pacific ocean. South America tends to experience less precipitation near the equator during austral winter, although the model mean produces increased rainfall following El Chichón. There is a dipole structure in the observed response during the first two L20 eruptions not captured in the model, although there is considerable spread among members in the generated composite (not shown).

Figure 6 illustrates that ModelE2-R reproduces the seasonal cycle of climatological rainfall (contoured) and oxygen isotope distribution (color) with some fidelity over South America. Where data permit (Fig. 6a) there is good agreement between model and observations, both displaying oxygen isotope DJF enrichment relative to JJA in the tropics north of the equator and the higher latitudes south of 30° S, and depletion in the continental interior south of the equator associated with the monsoon wet season. ModelE2-R (Fig. 6b) tends to produce too much DJF precipitation in far eastern Brazil although the seasonal migration of rainfall is well captured. This ability to accurately simulate the seasonality of $\delta^{18}O_p$ over the tropical Americas has also been noted in two atmospheric GCMs with no coupled ocean (NASA-GISS II and ECHAM-4, see Vuille et al., 2003).

Because of the considerable variability seen in observations and also across ensemble members, it is evident that a larger signal-to-noise ratio than is available from the L20 eruptions alone is required to help isolate any volcanic signal. ModelE2-R is the

laboratory from which we proceed to sample a larger number of events, some of which contain larger amplitude than the L20 eruptions.

3.2 Last millennium composites

3.2.1 Temperature and precipitation

s3.2.1

Figure 7 shows the LM post-volcanic temperature composite for all 48 events. During both seasons, cooling is statistically significant over virtually the entire continent (all spatial composites for the LM events are masked for significance at the 90 % level using a two-sided student t test). The temperature response is strongest in the interior of the continent, particularly during the austral winter. The enhanced high-latitude cooling exhibited in the observations does not emerge in the model composite.

The precipitation anomalies for the LM composite are shown in Fig. 8. As expected, there is a distinct seasonal structure in the response, with the largest anomaly concentrated in a narrow region north of the equator during austral winter. During JJA, precipitation increases in the North Atlantic region at the expense of a very strong and statistically significant precipitation reduction over the equator (including Northern Brazil, Ecuador, Venezuela, Colombia, and Guyana) and encompassing the northern Amazon Basin. This signal is consistent with a locally displaced ITCZ and a general weakening of the moisture flux owing to the decrease in saturation vapor pressure due to cooling that is demanded by Clausius–Clapeyron (Held and Soden, 2006). During this season, the precipitation response is significant virtually everywhere in northern South America. Supplement Fig. S5 further illustrates that the JJA precipitation response is remarkably robust to all eruptions that enter into the composite.

Figure 9b illustrates the relationship between area-averaged precipitation from 20° S–0° (DJF) and 0° to 12° N (JJA, these different regions were selected to reflect the seasonal migration of rainfall) and the maximum AOD encountered for each eruption. 16 eruptions are displayed with the three-member ensemble spread given for each.

All data is zonally averaged from 75 to 45° W. Precipitation only increases north of the equator during austral winter in a few model realizations. Moreover, the magnitude of the precipitation response during JJA scales with the size of the eruption, particularly for very large eruptions (e.g., comparing five eruptions with AOD > 0.3 vs. those with smaller perturbations, although the spread amongst the ensemble members is large). The spatial composite for each individual eruption (each averaged over the three ensemble members) is shown in Fig. S5.

The precipitation response during austral summer is more difficult to interpret (Fig. 8a). During this season, the zonally oriented Atlantic ITCZ migrates southward and the SACZ becomes more intense as it is connected with the area of convection over the central and southeastern part of the continent. It is noteworthy that the land cools substantially more than the surrounding ocean (Fig. 7), which one could expect to weaken the monsoon-sourced precipitation during DJF. While precipitation is indeed reduced over the tropical continent, the response is weaker than in JJA and less spatially coherent, with many areas failing to meet statistical significance. An analysis of the individual responses reveals that the signal is more eruption-dependent during DJF than during JJA (see Fig. S4), with a few events actually exhibiting modest increases in precipitation. Nonetheless, there is a clear tendency for reduced DJF precipitation within the SAMS region, although there is little to no dependence of the mean rainfall anomaly on the magnitude of the AOD perturbation, at least above the 0.1 threshold used in this study (Fig. 9b), unlike for equatorial South America during JJA. Conversely, the temperature response (Fig. 9a) depends on the size of the eruption in both seasons, as is expected.

3.2.2 Tropical hydroclimate response

Since the South American climate is intimately linked to large-scale tropical dynamics, the global precipitation composite is shown in Fig. S6 to better inform the model response. The most robust signal is characterized by a reduction in tropically averaged precipitation and the tendency for wet regions to become drier, and dry regions

to become wetter (see also Iles et al., 2013), in contrast to the anticipated hydrologic response in a future, higher-CO_2 world (Held and Soden, 2006).

This pattern is a thermodynamic effect linked to reduced moisture convergence within the convergence zones and to reduced moisture divergence in the descending zones of the Hadley cell, which reduces the contrast in values of precipitation – evaporation ($P - E$) between moisture convergence and divergence regions (Chou et al., 2009). The complete hydrologic response of the $\Delta P - E$ field (not shown) has the same spatial structure as the ΔP field, since evaporation is decreasing nearly everywhere in the tropics. Because both P and E are decreasing on the equator-ward flank of the ITCZ the $\Delta P - E$ signal is rather weak in the deep tropics, while $\Delta P - E$ increases more rapidly than ΔP in the subtropics.

The tendency for modest precipitation anomalies over the continent during DJF appears to be part of a pattern that spans a broad swath of longitudes across the entire deep tropics in association with the seasonal cycle. Nonetheless, the response during DJF is weaker over land.

3.2.3 Oxygen isotope anomalies

In order to relate the responses discussed in the previous sections back to a potentially observable paleoclimate metric, we show the composite $\Delta\delta^{18}O_p$ field for the DJF and JJA seasons in South America (Fig. 10). It should be cautioned that much of the isotopic variability that can be observed in proxies within the continental interior or high-elevation glacier sites will likely be seasonally biased toward the wet season months (Hardy et al., 2003).

During the JJA season, there is a strong enrichment of the $\delta^{18}O_p$ pattern that is zonally extended over equatorial South America. In addition, there is a corresponding $\delta^{18}O_p$ depletion in the adjacent North Atlantic sector. This response is inextricably coincident with the strong change in precipitation in the ITCZ domain that was assessed in Fig. 8, and is broadly consistent with a "rainfall amount" control on the isotopic imprint

(Dansgaard, 1964). South of approximately 15° S, the sign of the anomaly reverses to a depletion of the heavy isotope.

During the austral summer, volcanic eruptions lead to a clear negative excursion in $\delta^{18}O_p$ over virtually the entire SAMS region, including the Amazon basin, tropical Andes, and eastern Brazil. The statistical significance of the resulting isotopic anomaly extends throughout most of the landmass within the tropics and in the North Atlantic. There are small but non-significant exceptions (positive $\delta^{18}O_p$ excursions) such as in eastern Brazil. The negative excursions also include regions outside of the SAMS belt in the subtropics and mid-high latitudes of South America.

Remarkably, the austral summer $\delta^{18}O_p$ depletion is the opposite sign from what one would expect if the reduced precipitation were driving the isotopic response. Thus, it may well be that the strong temperature response to volcanic eruptions dominates the continent-wide oxygen isotope depletion during the DJF season and in the extratropics during JJA over the relatively weak precipitation response. Precipitation on the other hand appears to be the primary control knob of $\delta^{18}O_p$ during JJA within the ITCZ region.

In the case of volcanic forcing it appears that the amplitude of the temperature-response to volcanic eruptions over tropical South America is much larger than the rather weak and spatially incoherent precipitation signal. This may explain why the isotopic signal related to volcanic eruptions seems to respond primarily to atmospheric cooling, even in the tropics, where isotopic variability is usually more closely associated with changes in the hydrologic cycle.

Taken together, these results suggest that the primary controls on oxygen isotope variability are forcing and event-dependent, rather than being determined inherently by the latitude of interest (e.g., "precipitation driven" in the tropics and "temperature driven" in the extratropics). This conclusion is compelled by the fact that the precipitation production and distribution in proxy records are the result of an interaction between multiple scales of motion in the atmosphere, the temperature of air in which the condensate was embedded, and exchange processes operating from source to sink of the

parcel deposited at a site. Thus, a consistent description of how to interpret oxygen isotopes into a useful climate signal cannot be given without considering all of these processes and the target process of interest.

To further complement the spatial analysis, a composite Hovmöller diagram is utilized (Fig. 11) in order to illustrate the time-evolution of the temperature, precipitation, and oxygen isotope response. For this plot, the start of each eruption is defined as the closest January to the first month in which AOD reaches 0.1 in order to illustrate the seasonal evolution (rather than compositing by "month from each eruption" as in Fig. 3). Therefore, for all 48 events in the composite, the local AOD may reach this threshold within five months (before or after) of the January baseline point (eruptions in June are rounded up to the following January). The Hovmöller composites are plotted for ten years (beginning January three years prior to the eruption). The closest January point to the start of each eruption occurs in the 37th month of the Hovmöller (solid black line in Fig. 11a, b and d). Results are zonally averaged from 75° to 45° W, across the SAMS region.

Figure 11a demonstrates a substantial temperature anomaly that peaks south of 10° S (compare also to Fig. 7). The cooling lasts for several years following the eruption, and decays until much of the signal is lost ($\sim$ 4 years after the eruption at all latitudes). The zonally averaged peak reductions in South American precipitation anomalies occur over the tropical latitudes and last for a comparable period of time as the temperature response. The precipitation anomaly itself migrates synchronously with the seasonal cycle (red line in Fig. 11c maps out the latitude of maximum climatological precipitation averaged over all 30 year climatologies of each 48-member event, as a function of time of year). Figure 11b indicates that the largest precipitation response is confined to the equatorial regions during JJA, and any protrusion into mid-latitudes (still equatorward of the storm track), although weaker in magnitude, only occurs during the summer.

Figure 12 provides additional statistical insight into the magnitude of the excursions described in this section. Here, we sampled 100 random 48-event composites in a control simulation with no external forcing (each "event" two seasons in length defined as

an anomaly expressed relative to a surrounding climatology as done previously). The anomalies were averaged over the same areas as in Fig. 9, with different domains for DJF and JJA. Notably, for both seasons and for all three variables examined, the single 48-event post-volcanic composite (purple square) lies outside the distribution of all sampled 48-event composites constructed with no external forcing. Nonetheless, the distribution for a smaller sample of events (black circles denote the data for each (16) eruptions, each averaged over the three ensemble members) shows considerable spread.

3.2.4 Dynamics and extratropical and high-latitude influence

A number of studies have discussed the impact of volcanic forcing on high-latitude Southern Hemisphere dynamics (e.g., Robock et al., 2007; Karpechko et al., 2010; Wilmes et al., 2012; Gillett and Fyfe, 2013) with several potential consequences for South America. Like the ITCZ, the SACZ in particular is quite capable of exhibiting meridional displacements in response to external forcing. For example, Gonzalez et al. (2013) attributed a significant 20th century wetting trend in the SESA region during DJF to ozone forcing, supporting the notion of polar-driven changes in the subtropics (Kang et al., 2011). A similar trend may arise in the future if the SACZ moves poleward in concert with the large-scale circulation (Seth et al., 2010).

During the austral summer, Fig. 13 indicates a tendency for ModelE2-R to redistribute atmospheric mass toward higher latitudes during DJF and over the south Atlantic sector near South America during JJA. This pattern somewhat resembles the negative phase of the Southern Annular mode (SAM), although it exhibits a tripole structure and relatively weak signals in regions particularly important for SACZ dynamics. The precipitation anomalies spanning from the Southern Ocean to South America form a band-like pattern (not shown) that is anti-correlated with the sea level pressure signal although the direct impact of this extratropical influence appears rather modest over the South American continent. Additionally, the tropical easterlies from the North Atlantic that act as a conduit for moisture transport toward South America also

decrease in magnitude. The weakened moisture transport coupled with the thermodynamic effect of a cooler, drier atmosphere may explain the tendency for precipitation reductions over eastern Brazil and parts of the Amazon basin in most of the eruption events (Fig. S4) and in the LM composites, but there is no evidence for any substantial change in the dynamics that would change the source region for moisture and dominate the oxygen isotope excursions.

4 Conclusions

In this study, we have analyzed the response of temperature, precipitation, and $\delta^{18}O_p$ over South America to volcanic forcing during the 2nd half of the 20th century, and to many large tropical eruptions during the Last Millennium. It is now well known that volcanic eruptions lead to large-scale cooling throughout the tropics, and this result extends to most of the South American continent as well, except in regions that may be simultaneously affected by opposing ENSO behavior. In general, the precipitation response has been more enigmatic, though our results are in broad agreement with numerous other studies showing that there is a substantial decline in tropical-mean precipitation.

However, the immediate post-volcanic impact over South America has a complex seasonal and spatial structure. During the austral winter, the precipitation response over the continent is slaved to the response of the large-scale circulation, including a weakening of rainfall intensity within the ITCZ that is migrating northward. In the extratropics, the continent cools and exhibits slight precipitation declines nearly everywhere. Our results suggest the seasonal monsoon precipitation (during DJF) in ModelE2-R exhibits a fairly weak response that is scattered across the continent. It appears that volcanic forcing preconditions the tropical rainfall over the continent to decline during the wet season, but that this response is likely to be eruption-dependent and may be overwhelmed by internal variability.

A unique aspect of this study was to probe the $\delta^{18}O_p$ response to volcanic eruptions. During JJA, isotopes become heavily enriched in northern South America as convective activity produces substantially less precipitation. No such relation was found during the monsoon season, even within the tropics, where the large cooling appears to lead to more depleted $\delta^{18}O_p$, despite a weakened hydrologic cycle and reduced monsoon precipitation. In the extratropics, it appears that the temperature decline is driving isotopes toward more depleted values.

Unfortunately validation of our model results is hindered by the paucity of observational stable isotope data and by the coincidence of volcanic eruptions with ENSO events over the 20th century. Nonetheless our results may provide some guidance in the search of volcanic signals in high-resolution isotopic proxy data from South America. Given the importance of volcanic forcing for climate variability over the past millennium, and in particular the LIA period, which has been identified as a period of significant climatic perturbation in isotopic proxies from South America, a better understanding of the climatic response to volcanic forcing over this region is urgently needed.

The Supplement related to this article is available online at doi:10.5194/cpd-11-3375-2015-supplement.

Acknowledgements. This study was funded by NOAA C2D2 NA10OAR4310126 and NSF awards AGS-1003690 and AGS-1303828. We would like to thank NASA GISS for institutional support; resources supporting this work were provided by the NASA High-End Computing (HEC) Program through the NASA Center for Climate Simulation (NCCS) at Goddard Space Flight Center.

References

Anchukaitis, K. J., Buckley, B. M., Cook, E. R., Cook, B. I., D'Arrigo, R. D., and Ammann, C. M.: The influence of volcanic eruptions on the climate of the Asian monsoon region, Geophys. Res. Lett., 37, L22703, doi:10.1029/2010GL044843, 2010.

Apaéstegui, J., Cruz, F. W., Sifeddine, A., Vuille, M., Espinoza, J. C., Guyot, J. L., Khodri, M., Strikis, N., Santos, R. V., Cheng, H., Edwards, L., Carvalho, E., and Santini, W.: Hydroclimate variability of the northwestern Amazon Basin near the Andean foothills of Peru related to the South American Monsoon System during the last 1600 years, Clim. Past, 10, 1967–1981, doi:10.5194/cp-10-1967-2014, 2014.

Bird, B. W., Abbott, M. B., Rodbell, D. T., and Vuille, M.: Holocene tropical South American hydroclimate revealed from a decadally resolved lake sediment $\delta^{18}O$ record, Earth Planet. Sc. Lett., 310, 192–202, 2011.

Bradley, R. S., Vuille, M., Hardy, D. R., and Thompson, L. G.: Low latitude ice cores record Pacific sea surface temperatures, Geophys. Res. Lett., 30, 1174, doi:10.1029/2002GL016546, 2003.

Chen, M., Xie, P., Janowiak, J. E., and Arkin, P. A.: Global land precipitation: a 50-yr monthly analysis based on gauge observations, J. Hydrometeorol., 3, 249–266, 2002.

Chou, C., Neelin, J. D., Chen, C. A., and Tu, J. Y.: Evaluating the "rich-get-richer" mechanism in tropical precipitation change under global warming, J. Climate, 22, 1982–2005, 2009.

Coakley, J. A. and Grams, G. W.: Relative influence of visible and infrared optical properties of a stratospheric aerosol layer on the global climate, J. Appl. Meteorol., 15, 679–691, 1976.

Cole-Dai, J.: Volcanoes and climate, Wiley Interdisciplinary Reviews: Climate Change, 1, 824–839, 2010.

Cruz, F. W., Burns, S. J., Karmann, I., Sharp, W. D., Vuille, M., Cardoso, A. O., Ferrari, J. A., Dias, P. L. S., and Viana, O.: Insolation-driven changes in atmospheric circulation over the past 116,000 years in subtropical Brazil, Nature, 434, 63–66, 2005.

Crowley, T. J., Christe, T. A., and Smith, N. R.: Reassessment of Crete (Greenland) ice core acidity/volcanism link to climate change, Geophys. Res. Lett., 20, 209–212, 1993.

Crowley, T. J.: Causes of climate change over the past 1000 years, Science, 289, 270–277, 2000.

Crowley, T. J. and Unterman, M. B.: Technical details concerning development of a 1200 yr proxy index for global volcanism, Earth Syst. Sci. Data, 5, 187–197, doi:10.5194/essd-5-187-2013, 2013.
Dansgaard, W.: Stable isotopes in precipitation, Tellus, 16, 436–468, 1964.
D'Arrigo, R., Wilson, R., and Tudhope, A.: The impact of volcanic forcing on tropical temperatures during the past four centuries, Nat. Geosci., 2, 51–56, 2009.
da Silva, A. E. and de Carvalho, L. M. V.: Large-scale Index for South America Monsoon (LISAM), Atmos. Sci. Lett., 8, 51–57, 2007.
Driscoll, S., Bozzo, A., Gray, L. J., Robock, A., and Stenchikov, G.: Coupled Model Intercomparison Project 5 (CMIP5) simulations of climate following volcanic eruptions, J. Geophys. Res., 117, D17105, doi:10.1029/2012JD017607, 2012.
Emile-Geay, J., Seager, R., Cane, M. A., Cook, E. R., and Haug, G. H.: Volcanoes and ENSO over the past millennium, J. Climate, 21, 3134–3148, 2008.
Esper, J., Schneider, L., Krusic, P. J., Luterbacher, J., Büntgen U., Timonen, M., Sirocko, F., and Zorita, E.: European summer temperature response to annually dated volcanic eruptions over the past nine centuries, B. Volcanol., 75, 1–14, 2013.
Evan, A. T.: Atlantic hurricane activity following two major volcanic eruptions, J. Geophys. Res., 117, D06101, doi:10.1029/2011JD016716, 2012, 2012.
Fischer, E. M., Luterbacher, J., Zorita, E., Tett, S. F. B., Casty, C., and Wanner, H.: European climate response to tropical volcanic eruptions over the last half millennium, Geophys. Res. Lett., 34, L05707, doi:10.1029/2006GL027992, 2007.
Frierson, D. M. W., and Hwang, Y.: Extratropical influence On ITCZ shifts in slab ocean simulations of global warming, J. Climate, 25, 720–733, 2012.
Gao, C., Robock, A., and Ammann, C.: Volcanic forcing of climate over the past 1500 years: an improved ice core-based index for climate models, J. Geophys. Res., 113, D23111, doi:10.1029/2008JD010239, 2008.
Garreaud, R. D., Vuille, M., Compagnucci, R., and Marengo, J.: Present-day South American climate, Palaeogeogr. Palaeocl., 281, 180–195, 2009.
Gillett, N. P. and Fyfe, J. C.: Annular mode changes in the CMIP5 simulations, Geophys. Res. Lett., 40, 1189–1193, 2013.
Gillett, N. P., Weaver, A. J., Zwiers, F. W., and Wehner, M. F.: Detection of volcanic influence on global precipitation, Geophys. Res. Lett., 31, L12217, doi:10.1029/2004GL020044, 2004.

Gonzalez, P. L. M., Polvani, L. M., Seager, R., and Correa, G. J. P.: Stratospheric ozone depletion: a key driver of recent precipitation trends in south eastern South America, Clim. Dynam., 42, 1–18, 2013.
Goosse, H., Crowley, T., Zorita, E., Ammann, C., Renssen, H., and Driesschaert, E.: Modelling the climate of the last millennium: what causes the differences between simulations?, Geophys. Res. Lett., 32, L06710, doi:10.1029/2005GL22368, 2005.
Hammer, C. U., Clausen, H. B., and Dansgaard, W.: Greenland Ice Sheet evidence of postglacial volcanism and its climatic impact, Nature, 288, 230–235, 1980.
Hansen, J., Lacis, A., Ruedy, R., and Sato, M.: Potential climate impact of Mount Pinatubo eruption, Geophys. Res. Lett., 19, 215–218, 1992.
Hansen, J., Ruedy, R., Glascoe, J., and Sato, M.: GISS analysis of surface temperature change, J. Geophys. Res., 104, 30997–31022, 1999.
Hardy, D. R., Vuille, M., and Bradley, R. S.: Variability of snow accumulation and isotopic composition on Nevado Sajama, Bolivia, J. Geophys. Res., 108, 4693, 2003.
Harshvardhan and Cess, R. D.: Stratospheric aerosols: effect upon atmospheric temperature and global climate, Tellus, 28, 1–10, 1976.
Haywood, J. M., Jones, A., Bellouin, N., and Stephenson, D.: Asymmetric forcing from stratospheric aerosols impacts Sahelian rainfall, Nature Climate Change, 3, 660–665, 2013.
Hegerl, G. C., Crowley, T. J., Baum, S. K., Kim, K. Y., and Hyde, W. T.: Detection of volcanic, solar and greenhouse gas signals in paleo-reconstructions of Northern Hemispheric temperature, Geophys. Res. Lett., 30, 1242, doi:10.1029/2002GL016635, 2003.
Hegerl, G. C., Crowley, T. J., Hyde, W. T., and Frame, D. J.: Climate sensitivity constrained by temperature reconstructions over the past seven centuries, Nature, 440, 1029–1032, 2006.
Held, I. M. and Soden, B. J.: Robust responses of the hydrological cycle to global warming, J. Climate, 19, 5686–5699, 2006.
Hoffmann, G. and Heimann, M.: Water isotope modeling in the Asian monsoon region, Quatern. Int., 37, 115–128, 1997.
Huffman, G. J., Adler, R. F., Bolvin, D. T., and Gu, G.: Improving the global precipitation record: GPCP Version 2.1, Geophys. Res. Lett., 36, L17808, doi:10.1029/2009GL040000, 2009.
Iles, C. E., Hegerl, G. C., Schurer, A. P., and Zhang, X.: The effect of volcanic eruptions on global precipitation, J. Geophys. Res.-Atmos., 118, 8770–8786, 2013.
Joseph, R. and Zeng, N.: Seasonally modulated tropical drought induced by volcanic aerosol, J. Climate, 24, 2045–2060, 2011.

Kang, S., Polvani, L., Fyfe, J., and Sigmond, M.: Impact of polar ozone depletion on subtropical precipitation, Science, 332, 951–954, 2011.
Kang, S. M., Held, I. M., Frierson, D. M. W., and Zhao, M.: The response of the ITCZ to extratropical thermal forcing: idealized slab-ocean experiments with a GCM, J. Climate, 21, 3521–3532, 2008.
Kang, S. M., Frierson, D. M. W., and Held, I. M.: The tropical response to extratropical thermal forcing in an idealized GCM: the importance of radiative feedbacks and convective parameterization, J. Atmos. Sci., 66, 2812–2827, 2009.
Kanner, L. C., Burns, S. J., Cheng, H., and Edwards, R. L.: High-latitude forcing of the South American summer monsoon during the last glacial, Science, 335, 570–573, 2012.
Kanner, L. C., Burns, S. J., Cheng, H., Edwards, R. L., and Vuille, M.: High-resolution variability of the South American summer monsoon over the last seven millennia: insights from a speleothem record from the central Peruvian Andes, Quaternary Sci. Rev., 75, 1–10, 2013.
Kaplan, J. O., Krumhardt, K. M., Ellis, E. C., Ruddiman, W. F., Lemmen, C., and Goldewijk, K. K.: Holocene carbon emissions as a result of anthropogenic land cover change, Holocene, 21, 775–791, doi:10.1177/0959683610386983, 2010.
Karpechko, A. Y., Gillett, N. P., Dall'Amico, M., and Gray, L. J.: Southern Hemisphere atmospheric circulation response to the El Chichón and Pinatubo eruptions in coupled climate models, Q. J. Roy. Meteor. Soc., 136, 1813–1822, 2010.
Kirchner, I., Stenchikov, G. L., Graf, H.-F., Robock, A., and Antunña, J. C.: Climate model simulation of winter warming and summer cooling following the 1991 Mount Pinatubo volcanic eruption, J. Geophys. Res.-Atmos., 104, 19039–19055, 1999.
Krivova, N., Balmaceda, L., and Solanki, S.: Reconstruction of solar total irradiance since 1700 from the surface magnetic flux, Astron. Astrophys., 467, 335–346, 2007.
Lacis, A., Hansen, J., and Sato, M.: Climate forcing by stratospheric aerosols, Geophys. Res. Lett., 19, 1607– 1610, 1992.
Ledru, M.-P., Jomelli, V., Samaniego, P., Vuille, M., Hidalgo, S., Herrera, M., and Ceron, C.: The Medieval Climate Anomaly and the Little Ice Age in the eastern Ecuadorian Andes, Clim. Past, 9, 307–321, doi:10.5194/cp-9-307-2013, 2013.
Lucht, W., Prentice, I. C., Myneni, R. B., Sitch, S., Friedlingstein, P., Cramer, W., Bousquet, P., Buermann, W., and Smith, B.: Climatic control of the high-latitude vegetation greening trend and Pinatubo effect, Science, 296, 1687–1689, 2002.

Ludlow, F., Stine, A. R., Leahy, P., Murphy, E., Mayewski, P. A., Taylor, D., Killen, J., Baillie, M. G., Hennessy, M., and Kiely, G.: Medieval Irish chronicles reveal persistent volcanic forcing of severe winter cold events, 431–1649 CE, Environ. Res. Lett., 8, 024035, doi:10.1088/1748-9326/8/2/024035, 2013.
Man, W., Zhou, T., and Jungclaus, J. H.: Effects of large volcanic eruptions on global summer climate and East Asian monsoon changes during the last millennium: analysis of MPI-ESM simulations, J. Climate, 27, 7394–7409, 2014.
Mann, M. E., Cane, M. A., Zebiak, S. E., and Clement, A.: Volcanic and solar forcing of the tropical Pacific over the past 1000 years, J. Climate, 18, 447–456, 2005.
Marengo, J., Liebmann, B., Grimm, A., Misra, V., Silva Dias, P., Cavalcanti, I., Carvalho, L., Berbery, E., Ambrizzi, T., Vera, C. S., Saulo, A. C., Nogues-Paegle, J., Zipser, E., Seth, A., and Alves, L. M.: Recent developments on the South American monsoon system, Int. J. Climatol., 32, 1–21, 2012.
Marengo, J. A., Liebmann, B., Kousky, V. E., Filizola, N. P., and Wainer, I. C.: Onset and end of the rainy season in the Brazilian Amazon Basin, J. Climate, 14, 833–852, 2001.
Miller, G. H., Geirsdóttir, A'., Zhong, Y., Larsen, D. J., Otto-Bliesner, B. L., Holland, M. M., Bailey, D. A., Refsnider, K. A., Lehman, S. J., Southon, J. R., Anderson, C., Bjornsson, H., and Thordarson, T.: Abrupt onset of the Little Ice Age triggered by volcanism and sustained by sea-ice/ocean feedbacks, Geophys. Res. Lett., 39, doi:10.1029/2011GL050168, 2012.
Minnis, P., Harrison, E., Stowe, L., Gibson, G., Denn, F., Doelling, D., and Smith, W.: Radiative climate forcing by the Mount Pinatubo eruption, Science, 259, 1411–1415, 1993.
Neukom, R. and Gergis, J.: Southern Hemisphere high-resolution palaeoclimate records of the last 2000 years, Holocene, 22, 501–524, 2012.
Nogue's-Paegle, J. and Mo, K. C.: Alternating wet and dry conditions over South America during summer, Mon. Weather Rev., 125, 279–291, 1997.
Nogue's-Paegle, J., Mechoso, C. R., Fu, R., Berbery, E. H., Chao, W. C., Chen, T.-C., Cook, K., Diaz, A. F., Enfield, D., Ferreira, R., Grimm, A., Kousky, V., Liebmann, B., Marengo, J., Mo, K., Neelin, J. D., Paegle, J., Robertson, A., Seth, A., Vera, C., and Zhou, J.: Progress in Pan American CLIVAR research: understanding the South American monsoon, Meteorológica, 27, 1–30, 2002.
Novello, V. F., Cruz, F. W., Karmann, I., Burns, S. J., Stríkis, N. M., Vuille, M., Cheng, H., Lawrence Edwards, R., Santos, R. V., Frigo, E., and Barreto, E. A. S.: Multidecadal cli-

mate variability in Brazil's Nordeste during the last 3000 years based on speleothem isotope records, Geophys. Res. Lett., 39, doi:10.1029/2012GL053936, 2012.
Oman, L., Robock, A., Stenchikov, G., Schmidt, G. A., and Ruedy, R.: Climatic response to high-latitude volcanic eruptions, J. Geophys. Res.-Atmos., 110, D13103, doi:10.1029/2004JD005487, 2005.
Oman, L., Robock, A., Stenchikov, G. L., and Thordarson, T.: High-latitude eruptions cast shadow over the African monsoon and the flow of the Nile, Geophys. Res. Lett., 33, L18711, doi:10.1029/2006GL027665, 2006.
Peng, Y., Shen, C., Wang, W.-C., and Xu, Y.: Response of summer precipitation over eastern China to large volcanic eruptions, J. Climate, 23, 818–824, 2010.
Pollack, J. B., Toon, O. B., Sagan, C., Summers, A., Baldwin, B., and Van Camp, W.: Volcanic explosions and climatic change: a theoretical assessment, J. Geophys. Res., 81, 1071–1083, 1976.
Pollack, J. B., Toon, O. B., and Wiedman, D.: Radiative properties of the background stratospheric aerosols and implications for perturbed conditions, Geophys. Res. Lett., 8, 26–28, 1981.
Pongratz, J., Reick, C., Raddatz, T., and Claussen, M.: A Global Land Cover Reconstruction AD 800 to 1992: Technical Description, Rep. on Earth System Science, 51, Max Planck Institute for Meteorology, 72 pp., 2008.
Robock, A.: Volcanic eruptions and climate, Rev. Geophys., 38, 191–219, 2000.
Robock, A.: Volcanoes: role in climate, Encyclopedia of Atmospheric Sciences, 10, 2494–2500, 2003.
Robock, A. and Free, M. P.: Ice cores as an index of global volcanism from 1850 to the present, J. Geophys. Res.-Atmos., 100, 11549–11567, 1995.
Robock, A. and Mao, J.: Winter warming from large volcanic eruptions, Geophys. Res. Lett., 19, 2405–2408, 1992.
Robock, A. and Mao, J.: The volcanic signal in surface temperature observations, J. Climate, 8, 1086–1103, 1995.
Robock, A., Adams, T., Moore, M., Oman, L., and Stenchikov, G.: Southern Hemisphere atmospheric circulation effects of the 1991 Mount Pinatubo eruption, Geophys. Res. Lett., 34, L23710, doi:10.1029/2007GL031403, 2007.
Russell, G. L., Miller, J. R., and Rind, D.: A coupled atmosphere–ocean model for transient climate change studies, Atmos. Ocean 33, 683–730, 1995.

Sato, M., Hansen, J. E., McCormick, M. P., and Pollack, J. B.: Stratospheric aerosol optical depths, 1850–1990, J. Geophys. Res.-Atmos., 98, 22987–22994, 1993.
Schmidt, G. A., LeGrande, A. N., and Hoffmann, G.: Water isotope expressions of intrinsic and forced variability in a coupled ocean–atmosphere model, J. Geophys. Res.-Atmos., 112, D10103, doi:10.1029/2006JD007781, 2007.
Schmidt, G. A., Jungclaus, J. H., Ammann, C. M., Bard, E., Braconnot, P., Crowley, T. J., Delaygue, G., Joos, F., Krivova, N. A., Muscheler, R., Otto-Bliesner, B. L., Pongratz, J., Shindell, D. T., Solanki, S. K., Steinhilber, F., and Vieira, L. E. A.: Climate forcing reconstructions for use in PMIP simulations of the last millennium (v1.0), Geosci. Model Dev., 4, 33–45, doi:10.5194/gmd-4-33-2011, 2011.
Schmidt, G. A., Jungclaus, J. H., Ammann, C. M., Bard, E., Braconnot, P., Crowley, T. J., Delaygue, G., Joos, F., Krivova, N. A., Muscheler, R., Otto-Bliesner, B. L., Pongratz, J., Shindell, D. T., Solanki, S. K., Steinhilber, F., and Vieira, L. E. A.: Climate forcing reconstructions for use in PMIP simulations of the Last Millennium (v1.1), Geosci. Model Dev., 5, 185–191, doi:10.5194/gmd-5-185-2012, 2012.
Schmidt, G. A., Kelley, M., Nazarenko, L., Ruedy, R., Russell, G. L., Aleinov, I., Bauer, M., Bauer, S., Bhat, M. K., Bleck, R., Canuto, V., Chen, Y., Cheng, Y., Clune, T. L., DelGenio, A., de Fainchtein, R., Faluvegi, G., Hansen, J. E., Healy, R. J., Kiang, N. Y., Koch, D., Lacis, A. A., LeGrande, A. N., Lerner, J., Lo, K. K., Matthews, E. E., Menon, S., Miller, R. L., Oinas, V., Oloso, A., Perlwitz, J., Puma, M. J., Putman, W. M., Rind, D., Romanou, A., Sato, M., Shindell, D. T., Sun, S., Syed, R., Tausnev, N., Tsigaridis, K., Unger, N., Voulgarakis, A., Yao, M.-S., and Zhang, J.: Configuration and assessment of the GISS ModelE2 contributions to the CMIP5 archive, J. Adv. Model. Earth Syst., 6, 141–184, 2014a.
Schmidt, G. A., Annan, J. D., Bartlein, P. J., Cook, B. I., Guilyardi, E., Hargreaves, J. C., Harrison, S. P., Kageyama, M., LeGrande, A. N., Konecky, B., Lovejoy, S., Mann, M. E., Masson-Delmotte, V., Risi, C., Thompson, D., Timmermann, A., Tremblay, L.-B., and Yiou, P.: Using palaeo-climate comparisons to constrain future projections in CMIP5, Clim. Past, 10, 221–250, doi:10.5194/cp-10-221-2014, 2014b.
Schurer, A. P., Tett, S. F., and Hegerl, G. C.: Small influence of solar variability on climate over the past millennium, Nat. Geosci., 7, 104–108, 2014.
Seth, A., Rojas, M., and Rauscher, S. A.: CMIP3 projected changes in the annual cycle of the South American Monsoon, Climatic Change, 98, 331–357, 2010.

Shindell, D. T., Schmidt, G. A., Mann, M. E., and Faluvegi, G.: Dynamic winter climate response to large tropical volcanic eruptions since 1600, J. Geophys. Res.-Atmos., 109, D05104, doi:10.1029/2003JD004151, 2004.

Steinhilber, F., Beer, J., and Fröhlich, C.: Total solar irradiance during the Holocene, Geophys. Res. Lett., 36, L19704, doi:10.1029/2009GL040142, 2009.

Stenchikov, G., Hamilton, K., Robock, A., Ramaswamy, V., and Schwarzkopf, M. D.: Arctic oscillation response to the 1991 Pinatubo eruption in the SKYHI general circulation model with a realistic quasi-biennial oscillation, J. Geophys. Res.-Atmos., 109, D03112, doi:10.1029/2003JD003699, 2004.

Stenchikov, G., Hamilton, K., Stouffer, R. J., Robock, A., Ramaswamy, V., Santer, B., and Graf, H.-F.: Arctic Oscillation response to volcanic eruptions in the IPCC AR4 climate models, J. Geophys. Res.-Atmos., 111, D07107, doi:1029/2005JD006286, 2006.

Stenchikov, G. L., Kirchner, I., Robock, A., Graf, H.-F., Antuna, J. C., Grainger, R., Lambert, A., and Thomason, L.: Radiative forcing from the 1991 Mount Pinatubo volcanic eruption, J. Geophys. Res.-Atmos., 103, 13837–13857, 1998.

Stothers, R. B. and Rampino, M. R.: Historic volcanism, European dry fogs, and Greenland acid precipitation, 1500 BC to AD 1500, Science, 222, 411–413, 1983.

Thompson, L. G., Mosley-Thompson, E., Davis, M. E., Lin, P.-N., Henderson, K. A., Cole-Dai, J., Bolzan, J. F., and Liu, K.-B.: Late glacial stage and Holocene tropical ice core records from Huascaran, Peru, Science, 269, 46–50, 1995.

Thompson, L. G., Davis, M., Mosley-Thompson, E., Sowers, T. A., Henderson, K. A., Zagorodnov, V. S., Lin, P. N., Mikhalenko, V. N., Campen, R. K., Bolzan, J. F., Cole-Dai, J., and Francou, B.: A 25 000-year tropical climate history from Bolivian ice cores, Science, 282, 1858–1864, 1998.

Thompson, L. G., Mosley-Thompson, E., Brecher, H., Davis, M., León, B., Les, D., Lin, P.-N., Mashiotta, T., and Mountain, K.: Abrupt tropical climate change: past and present, P. Natl. Acad. Sci. USA, 103, 10536–10543, 2006.

Timmreck, C.: Modeling the climatic effects of large explosive volcanic eruptions, Wiley Interdisciplinary Reviews: Climate Change, 3, 545–564, 2012.

Trenberth, K. E. and Dai, A.: Effects of Mount Pinatubo volcanic eruption on the hydrological cycle as an analog of geoengineering, Geophys. Res. Lett., 34, L15702, doi:10.1029/2007GL030524, 2007.

Turco, R., Whitten, R., and Toon, O.: Stratospheric aerosols: observation and theory, Rev. Geophys., 20, 233–279, 1982.

Van Breukelen, M., Vonhof, H., Hellstrom, J., Wester, W., and Kroon, D.: Fossil dripwater in stalagmites reveals Holocene temperature and rainfall variation in Amazonia, Earth Planet. Sc. Lett., 275, 54–60, 2008.

Vera, C., Higgins, W., Amador, J., Ambrizzi, T., Garreaud, R., Gochis, D., Gutzler, D., Lettenmaier, D., Marengo, J., Mechoso, C. R., Nogues-Paegle, J., Silva Dias, P. L., and Zhang, C.: Toward a unified view of the American monsoon systems, J. Climate, 19, 4977–5000, 2006.

Vimeux, F., Gallaire, R., Bony, S., Hoffmann, G., and Chiang, J. C.: What are the climate controls on δD in precipitation in the Zongo Valley (Bolivia)? Implications for the Illimani Ice Core interpretation, Earth Planet. Sc. Lett., 240, 205–220, 2005.

Vimeux, F., Ginot, P., Schwikowski, M., Vuille, M., Hoffmann, G., Thompson, L. G., and Schotterer, U.: Climate variability during the last 1000 years inferred from Andean ice cores: a review of methodology and recent results, Palaeogeogr., Palaeocl., 281, 229–241, 2009.

Vuille, M. and Werner, M.: Stable isotopes in precipitation recording South American summer monsoon and ENSO variability: observations and model results, Clim. Dynam., 25, 401–413, 2005.

Vuille, M., Bradley, R. S., Werner, M., Healy, R., and Keimig, F.: Modeling δ^{18}O in precipitation over the tropical Americas: 1. Interannual variability and climatic controls, J. Geophys. Res.-Atmos., 108, 4174, doi:10.1029/2001JD002038, 2003.

Vuille, M., Burns, S. J., Taylor, B. L., Cruz, F. W., Bird, B. W., Abbott, M. B., Kanner, L. C., Cheng, H., and Novello, V. F.: A review of the South American monsoon history as recorded in stable isotopic proxies over the past two millennia, Clim. Past, 8, 1309–1321, doi:10.5194/cp-8-1309-2012, 2012.

Wilmes, S. B., Raible, C. C., and Stocker, T. F.: Climate variability of the mid- and high-latitudes of the Southern Hemisphere in ensemble simulations from 1500 to 2000 AD, Clim. Past, 8, 373–390, doi:10.5194/cp-8-373-2012, 2012.

Yoshimori, M., Stocker, T. F., Raible, C. C., and Renold, M.: Externally forced and internal variability in ensemble climate simulations of the Maunder Minimum, J. Climate, 18, 4253–4270, 2005.

Zhang, D., Blender, R., and Fraedrich, K.: Volcanoes and ENSO in millennium simulations: global impacts and regional reconstructions in East Asia, Theor. Appl. Climatol., 111, 437–454, 2013.

Zhou, J. and Lau, K.: Does a monsoon climate exist over South America?, J. Climate, 11, 1020–1040, 1998.

Zielinski, G. A.: Stratospheric loading and optical depth estimates of explosive volcanism over the last 2100 years derived from the Greenland Ice Sheet Project 2 ice core, J. Geophys. Res.-Atmos., 100, 20 937–20 955, 1995.

Zielinski, G. A.: Use of paleo-records in determining variability within the volcanism–climate system, Quaternary Sci. Rev., 19, 417–438, 2000.

Table 1. Time of Eruptions and Global Aerosol Optical Depth (AOD) from Crowley and Unterman (2013). List of LM eruptions.

Start date of eruption[a]	Seasons in LM composite		Max AOD[b]
	DJF[c]	JJA	
Jan 971	972	971–972	0.22
Jan 1193	1194	1193–1194	0.18
Jul 1228	1229–1251	1229–1230	0.38
Oct 1257	1258–1260	1258–1259	0.69
Jan 1286	1287–1288	1286–1287	0.28
Jul 1455	1456–1458	1456–1458	0.44
Jan 1600	1601	1600	0.17
Jan 1641	1642	1641–1642	0.23
May 1673	1674	1674	0.21
Apr 1694	1695–1697	1694–1696	0.24
Jan 1809	1810–1811	189–1810	0.30
May 1815	1816–1818	1815–1817	0.47
May 1835	1836	1835–1836	0.23
Jan 1883	1884	1884	0.20
Apr 1963	1964	1964	0.12
Apr 1982[d]			0.11
Jun 1991	1992	1992	0.18

[a] Start of Eruption dates based on when they can be identified in the Crowley/Sato time-series averaged over the latitude band from 30° S to 20° N. May be slightly different than actual eruption date.

[b] Maximum AOD over the 30° S to 20° N latitude band encountered in monthly time-series during the duration of each event.

[c] December in year prior to listed date.

[d] El Chichón not included in LM composites.

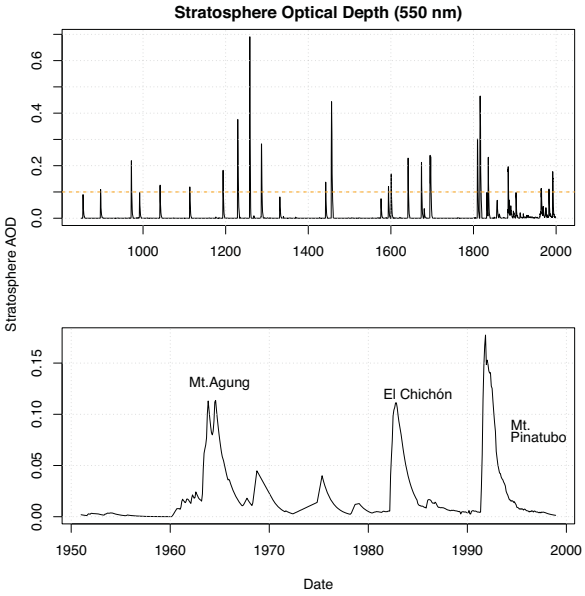

Figure 1. Aerosol Optical Depth (AOD) used to force the NASA GISS ModelE2-R over the Last Millennium and (bottom) focused on 1950–1999 (Crowley and Sato) as discussed in text. AOD is the vertically integrated (15–35 km) and latitudinal average from 30° S to 20° N. Note difference in vertical scale between graphs. Orange dashed line marks the AOD threshold for defining a LM eruption in the present study. Eruption events defined in text must sustain the threshold AOD for at least one year, so not all events above the orange dashed line are used in the composites.

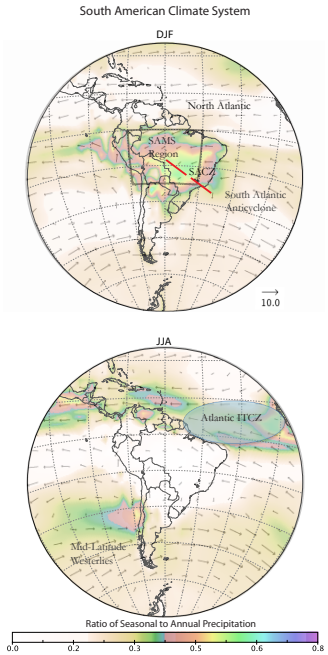

Figure 2. Cartoon sketch of the South American climate system. SAMS box is drawn over the domain from 75° to 45° W, 20° S to 0° and used for Figs. 9 and 12. Filled color indicates the ratio of precipitation that falls during the selected season to the entire year (December–November). Values for the precipitation ratio, and for the wind field (850 hPa in $m s^{-1}$), are averages from 48 selected 30 year climatologies during the Last Millennium simulations that surround volcanic eruption events (16 eruptions within three ensemble members) that are used for the Last Millennium composites.

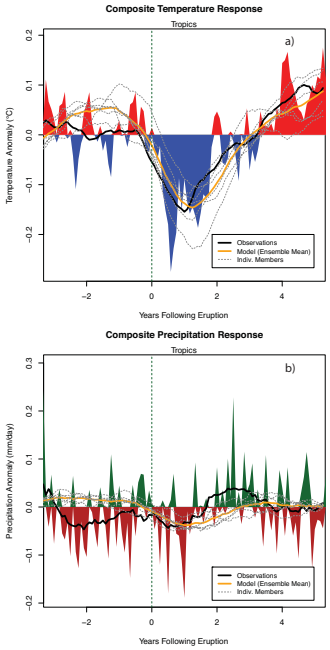

Figure 3. Composite tropical (25° S to 25° N) response in **(a)** Temperature and **(b)** Precipitation using El Chichón and Mt. Pinatubo. Fill color denotes monthly observed anomalies using **(a)** GISTEMP and **(b)** GPCP products with 18 month running average in observations (solid black), ModelE2-R ensemble mean (solid orange), and six individual ensemble members (dashed grey). Anomalies base-lined to give a mean of zero over displayed period.

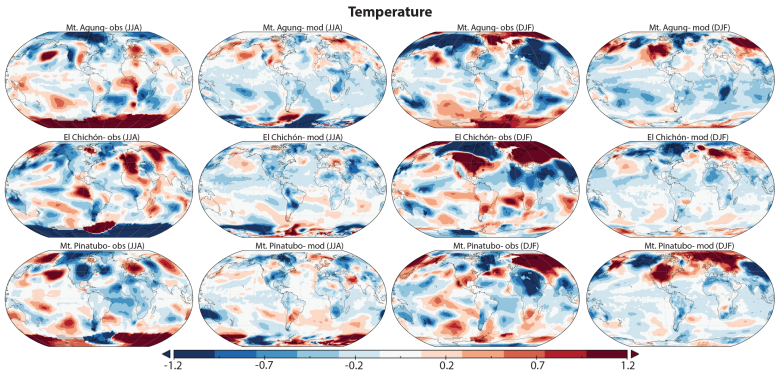

Figure 4. Temperature change (°C) for each L20 eruption (labeled on plot) for JJA in GISTEMP (first column), model (second column), and during DJF for GISTEMP (third column) and model (fourth column). All plots use ENSO-removal procedure described in text and the model results are shown for six-member ensemble mean.

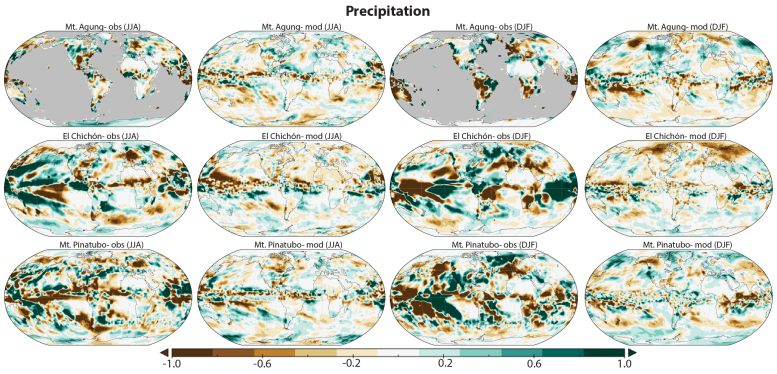

Figure 5. As in Fig. 4, except for Precipitation change (mm day^{-1}).

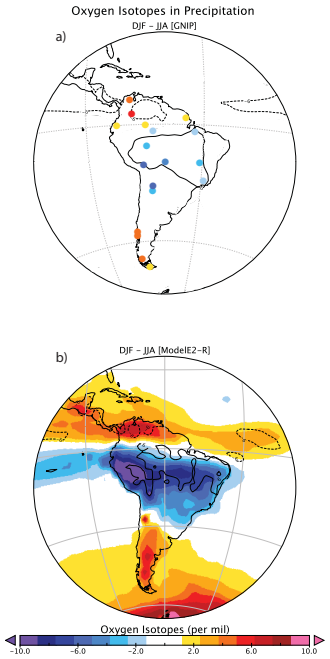

Figure 6. Seasonal cycle (DJF minus JJA) of $\delta^{18}O_p$ in **(a)** GNIP and **(b)** ModelE2-R (colored). Precipitation is contoured in solid at 6 mm day^{-1} and dashed at −6 mm day^{-1}. GNIP data selected with a minimum of 70 reported $\delta^{18}O_p$ values at a given station from 1960–present. Model precipitation and $\delta^{18}O_p$ climatology from 1960–2005 and GPCP precipitation over the same period (1979–2005 over ocean).

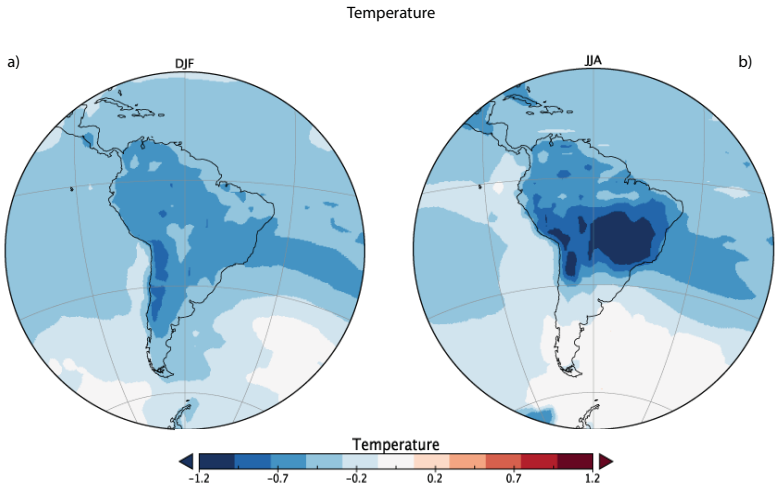

Figure 7. Last Millennium post-volcanic temperature composite (°C) averaged over all 48 events during **(a)** DJF and **(b)** JJA from GISS ModelE2-R using procedure described in text.

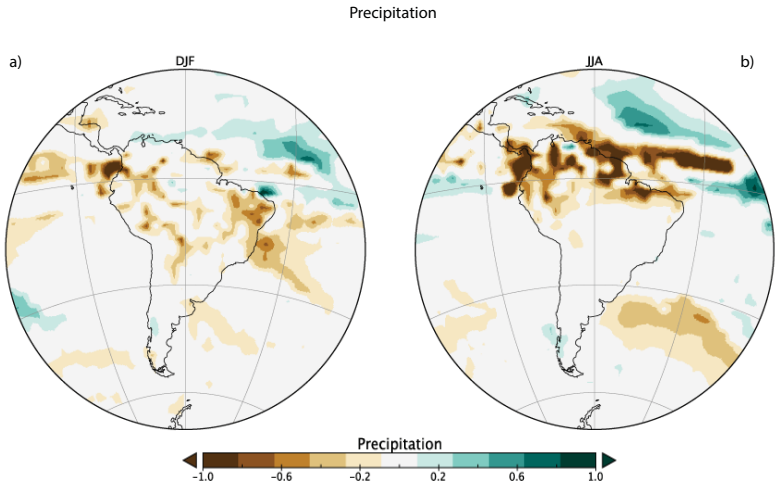

Figure 8. Last Millennium post-volcanic precipitation composite (mm day^{-1}) with all eruption events during **(a)** DJF and **(b)** JJA from GISS ModelE2-R using procedure described in text.

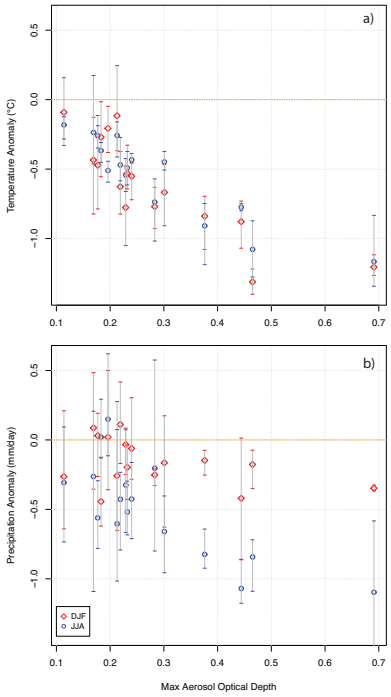

Figure 9. (a) Average temperature during DJF within the SAMS region (red, 75° to 45° W, 20° S to 0° N) and equatorial South America during JJA (blue, 75° to 45° W, 0 to 12° N) plotted against the peak AOD for all 16 eruptions (each point averaged over three ensemble members with the three member spread shown as horizontal bars) and **(b)** for precipitation.

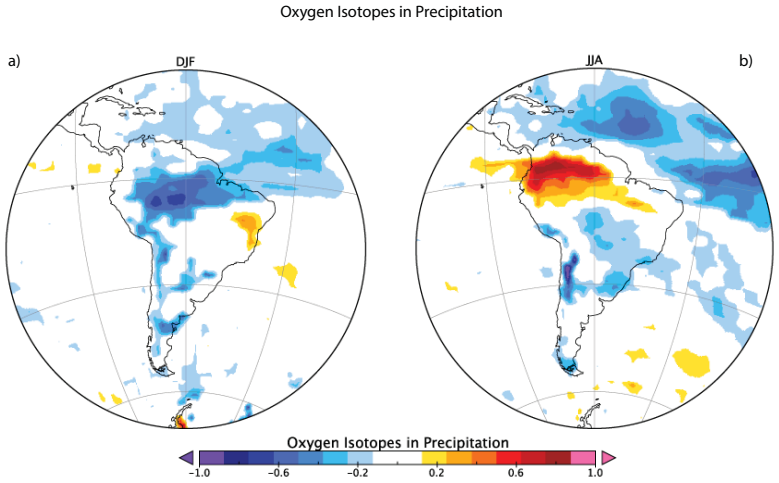

Figure 10. Last Millennium post-volcanic oxygen isotope in precipitation ($\delta^{18}O_p$) composite (per mil) with all eruption events during **(a)** DJF and **(b)** JJA from GISS ModelE2-R using procedure described in text.

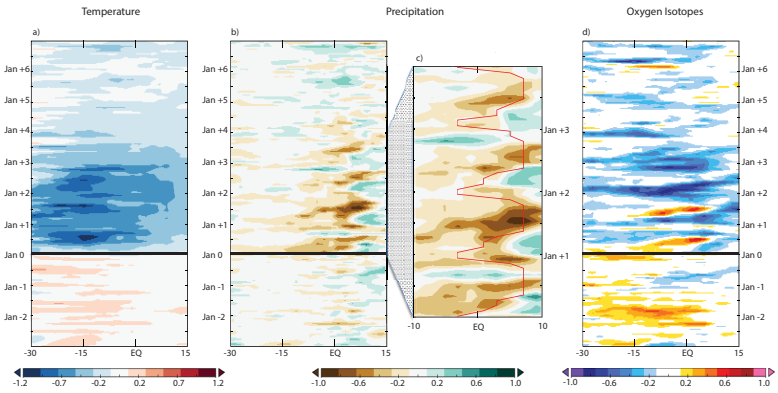

Figure 11. Last Millennium Hovmöller diagram (10 years, time moving forward going upward, with year number labeled next to each month) for **(a)** temperature anomaly (°C) **(b)** precipitation anomaly (mm day^{-1}) using procedure described in text. Solid black lines mark closest January to start of each eruption used in composite. **(c)** Same as panel **(b)**, except zoomed in on 10° S to 10° N and over 3 years of time beginning with the January closest to each eruption. Red line in panel c shows latitude of maximum climatological precipitation as a function of time of year. All results zonally averaged in model from 76.25° to 46.75° W. **(d)** Last millennium Hovmöller diagrams for oxygen isotopes in precipitation (‰).

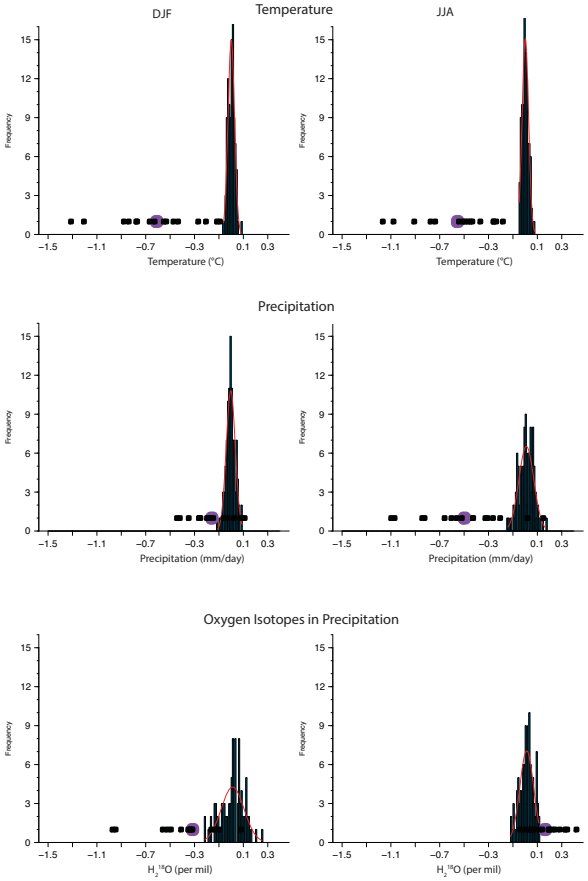

Figure 12. Frequency distribution of 100 random 48-event composites in LM control simulation of ModelE2-R (blue) for temperature (top row), precipitation (middle), and oxygen isotopes in precipitation (bottom) for DJF (left column) and JJA (right column). Results averaged over same domains as in Fig. 9. Normal distribution with a mean and standard deviation equal to that of the data shown in red. Purple square shows the single 48-event composite used in this study, with the distribution of individual 16 volcanic eruptions (each averaged over three ensemble members) in black dots.

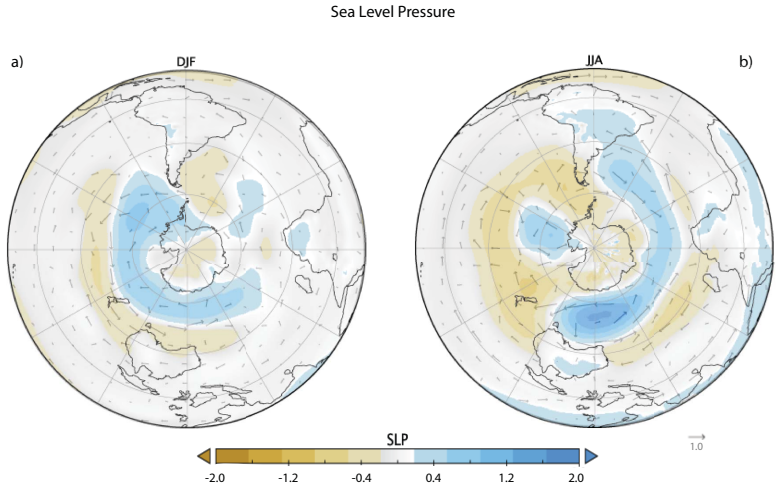

Figure 13. Post-volcanic LM composite of Sea Level Pressure (SLP, hPa) anomaly for **(a)** DJF **(b)** JJA (vector magnitude below plot, $m\,s^{-1}$).